

# On the balance between the tonal and broadband noise of isolated propellers

International Journal of Aeroacoustics

XX(X):3–49

©The Author(s) 2016

Reprints and permission:

[sagepub.co.uk/journalsPermissions.nav](http://sagepub.co.uk/journalsPermissions.nav)

DOI: 10.1177/ToBeAssigned

[www.sagepub.com/](http://www.sagepub.com/)

SAGE

Deepak C Akiwate<sup>1</sup>, Phillip Joseph<sup>2</sup>, **Anthony Parry<sup>3</sup>**, and  
Chaitanya Paruchuri<sup>4</sup>

---

## Abstract

This study presents a predominantly numerical and theoretical investigation into the balance of tonal and broadband noise due to an isolated propeller in uniform motion. The predicted trends in the balance between tonal and broadband noise radiation with varying blade number and speed of rotation is supported by preliminary experimental measurements. Here, we assume that the dominant noise generation mechanisms are the tones due to steady loading and blade thickness, while the broadband noise is due to boundary layer scattering at the trailing edge. The study also provides a detailed comparison between the tonal and broadband formulations to highlight their similarities and differences. In this paper, we show that the main differences in the behaviour and character of the tonal and broadband spectra and directivities are due to the number of acoustic modes that can be excited.

This paper presents a parametric study in which the variation in tonal and broadband noise is investigated as a function of blade tip Mach number ( $M_t$ ) and blade number ( $B$ ) whilst maintaining constant solidity and thrust. This study is repeated for three NACA airfoil profiles. It is found that tonal noise dominates at low blade number and low frequency and/or higher tip speeds, while broadband noise is the major contributor at high-frequencies and at high blade number and low tip speeds. The results show a clear distinction between the combinations of  $M_t$  and  $B$  that are dominated by tonal and by broadband noise. These results are interpreted from fundamental principles relating to modal radiation efficiencies. We confirm this trend of balance between tonal and broadband noise with measured noise at different  $B$  and  $M_t$ . The results of this paper will serve as useful guidelines for preliminary propeller design.

## Keywords

Propeller noise, tonal and broadband noise, Self-noise

---

## Objectives & scope of the paper

The propeller noise spectrum comprises the sum of tonal and broadband components. The balance between them affects, not only the overall noise level, but the psycho-acoustic impression of the noise, with tonal noise generally being regarded as more 'annoying' than broadband noise. The main objective and scope of this paper is to investigate numerically the balance between the tonal and broadband noise due to an isolated propeller. The numerical study will employ existing, relatively simple analytical noise models based on flat plate theory to predict the blade response and numerical and empirical models to predict the boundary layer flow. We emphasise that our objective in this paper is *not* to make highly accurate noise predictions, which could be more easily achieved with more sophisticated propeller noise models such as Farassat<sup>1</sup> or high-fidelity numerical models such as Chirico et al.<sup>2</sup>, but simply to elucidate the factors that control the balance between tonal and broadband propeller self-noise. This predictions presented in this paper are therefore mostly qualitative, aimed at assessing and understanding the factors that control the balance between tonal and broadband propeller noise.

In this paper we focus on the essential similarities of the analytical formulations of tonal and broadband propeller noise and demonstrate that the differences in behaviour

---

<sup>1</sup>Research Fellow, ISVR, University of Southampton, UK

<sup>2</sup>Professor, ISVR, University of Southampton, UK

<sup>3</sup>Consultant, ISVR, University of Southampton, UK

<sup>4</sup>Associate professor and RAEng Research fellow, ISVR, University of Southampton, UK

### Corresponding author:

Phillip Joseph, Institute of Sound and Vibration Research, University of Southampton, Southampton, UK, SO17 1BJ.

Email: pfj@soton.ac.uk

between them due to variations in blade number and tip speed can be attributed to the number of acoustic modes that are able to be excited.

The formulation for the tonal radiation due to an isolated propeller by Parry<sup>3</sup> and the broadband formulation by Blandeau<sup>4</sup> will be employed to explain the differences in tonal and broadband propeller noise with variations in blade number and tip speed.

The current paper is a detailed study of the factors that influence the balance between the tonal and broadband noise from uninstalled open rotors in uniform motion. It builds on the preliminary work of Akiwate et al.<sup>5</sup>, but now includes realistic airfoil profiles and the use of an iterative method to compute the correct distributions of lift and drag coefficients using the panel method code XFOIL<sup>6</sup>. In this paper, the three different airfoil geometries; symmetric NACA0012, and high cambered NACA4312 and NACA6312, are investigated. This paper describes the results of a parametric study of the predicted tonal and broadband noise obtained by systematically varying blade number and tip speed while maintaining constant blade solidity and thrust. These parameters will be varied around those of a baseline airfoil defined to have the same blade diameter and takeoff tip speed as the ATR42 propeller<sup>7,8</sup> but with blade profiles taken from an aerodynamic optimisation study by Klein<sup>9</sup>, since the detailed profiles of the ATR42 propeller have not been published. This paper will conclude with preliminary guidelines on the choice of blade number and tip speed required for low-noise propellers for a particular blade profile at a fixed blade solidity and thrust. This paper will demonstrate that this low noise condition occurs at high blade number and low tip speed, where broadband noise dominates.

## **Background**

In recent years, global annual air traffic has increased significantly, resulting in a significant increase in environmental concerns relating to noise emissions<sup>10</sup>. The

---

International Civil Aviation Organization (ICAO) has set strict regulations regarding future targets for aircraft noise emissions. Due to the emergence of electric and distributed propulsion systems, there has also been growing interest in replacing turbofan engines with propellers in regional aircraft, Urban Air Mobility (UAM), and propeller drones. Open rotor technology provides high efficiency at moderate flight speeds<sup>3</sup>. However, these vehicles will fly close to cities raising concerns about environmental noise, which may negatively impact on their public acceptability. With the development of open-rotor technology and the potential increase in urban air traffic, monitoring agencies are likely to impose stringent regulations on noise levels from propeller-driven air vehicles.

The noise generated by an uninstalled propeller can be categorized as either tonal or broadband in nature<sup>11</sup>. Tonal noise is attributed to the periodic loading and mass displacement by the thickness of the rotating propeller, while broadband noise is predominantly due to the turbulent boundary layer on the blade surface passing over the trailing edge<sup>3,12</sup> as shown in Fig. 1. [Figure 1 shows the propeller moving with the forward flight Mach number \( \$M\_x\$ \) and its associated noise sources.](#) The relative contributions from each source to overall noise depend on the blade geometry, blade number, flight speed, and blade tip Mach number. This balance between tonal and broadband noise is the main objective of this paper.

Substantial literature is available for predicting the tonal noise due to open rotors<sup>3,13–18</sup>. One of the earliest studies was performed by Gutin<sup>13</sup> by considering the blades as rotating point forces. Later, a more realistic approach was presented by Hanson using helicoidal surface theory. This formulation explicitly takes into account blade sweep and offset. Later, Parry<sup>3</sup> extended the propeller noise prediction scheme and developed a formulation for the noise due to counter-rotating propellers. Theoretical models aimed at the prediction of the broadband trailing self-noise edge noise from

isolated propellers also has a long history beginning with <sup>4,19-21</sup>. One of most recent contributions to the analytical prediction of trailing edge self-noise from isolated propellers is due to Blandeau <sup>4</sup> whose formulation is similar to that of Kim and George <sup>19</sup>, but includes non-compactness effects of the source distribution along the chord <sup>4,22</sup>.

To the authors' knowledge, limited literature is available investigating the balance between open propellers' tonal and broadband noise. Gojon et al. <sup>23</sup> performed an experimental investigation into the relative contributions to overall noise due to tones and broadband noise of a small, low-speed APC (APC 9 × 6 SF, APC 11 × 4.7 SF) and ISAE 2-5 (diameter = 0.23-0.28m, chord = 0.025m) propellers whose Reynolds numbers  $Re_{tip}$  are of the order of  $O(10^4)$  to  $O(10^5)$  are therefore considerably smaller than those of full-scale aircraft propellers  $O(10^6)$  to  $O(10^7)$ . The number of blades was varied between 2 and 5. They concluded that overall Sound Pressure Level was reduced by 10dB in the plane of rotation by increasing the number of blades from 2 to 5 although a significant increase in broadband noise was also observed, suggesting that tones were the dominant source for this propeller configuration. However, we note that this experimental parametric study did not attempt to maintain thrust or blade solidity.

Recently, Greenwood et al. <sup>24</sup> presented predictions of the balance of tones and broadband noise using their analytical prediction code for an eVTOL propeller in the "hover" operating condition at a fixed thrust of 2500 N. The rotor had a diameter of 3 m with a solidity of 0.2. The tip Mach number varied from 0.3 (near stall) to 0.8, and tonal noise increased by more than 50dB over this range of tip speeds while the broadband noise varied by less than 8dB. Broadband noise was found to be greatest at the lowest tip speeds due to flow separation over the blades. More recently, Akiwate et al. <sup>5</sup> have attempted to understand the factors that affect the balance between the tonal and broadband self-noise contributions from an uninstalled open rotor using existing analytic propeller noise models developed at the [Institute of Sound and Vibration Research](#)

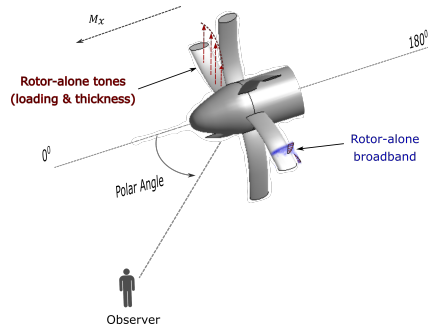


**Figure 1.** Sources of propeller noise<sup>5</sup>.

(ISVR) presented below within a consistent theoretical framework. A parametric study was performed into the balance of tonal and broadband noise due to variations in blade number and tip speed while maintaining constant thrust and blade solidity. However, this preliminary study was restricted to NACA0012 airfoil profiles with the effects of local Angle of Attack ( $\alpha_a$ ) neglected and the use of approximate estimates for the lift and drag coefficients.

## Theoretical Analysis

This section reviews existing analytic and semi-empirical models for predicting the tonal and broadband far-field noise due to an uninstalled propeller. The dominant sources of tonal noise are assumed to be due to steady loading and thickness effects, while the broadband noise is assumed to be due entirely to the self-noise case caused by the scattering of the turbulent boundary layer at the trailing edge. The analytic models will be presented within a consistent theoretical framework to highlight the similarities and differences between the two noise generation mechanisms. The models are based on classical isolated flat plate theory using the model developed by Parry<sup>3</sup> for the loading and thickness tonal noise, and Amiet<sup>25,26</sup> for the broadband noise to compute the unsteady blade response.

Using strip theory, the broadband noise prediction model treats spanwise variations in unsteady blade loading and blade geometry. The model uses an input the boundary layer pressure spectrum at the trailing edge, which we estimate using the empirical model due to Rozenberg<sup>27</sup> whose boundary layer parameters are estimated from the panel method code XFOIL<sup>6</sup>. Note that the methods used for predicting tonal and broadband noise have been validated and discussed in previous studies<sup>3,4,22,28</sup>. We start with an overview of the basic calculations of the propeller thrust based on classical blade element theory.

### Propeller calculations

The total thrust produced by the propeller with  $B$  blades is estimated by integrating the local thrust  $dT(r)$  produced by a small element (shown in Fig. 2) along the span from the hub radius  $r_h$  to the tip radius  $R_t$  as;

$$T = \int_{r_h}^{R_t} 1/2 \rho U_r^2 c [C_L \cos(\theta_f) - C_D \sin(\theta_f)] B dr \quad (1)$$

where  $C_L(r)$ ,  $C_D(r)$  are the lift and drag coefficient for the blade element, respectively,  $c(r)$  is the local chord and  $U_r(r)$  is the sectional incoming velocity in the blade frame of reference and given by  $\sqrt{V_0^2(r) + V_t^2(r)}$  where  $V_0(r)$  and  $V_t(r)$  are the axial and rotational components of the flow for the section, respectively.

The local angle of incidence  $\alpha_a$  at any radial position  $r$  is calculated from the difference between the blade pitch and the flow angle  $\theta_f = 90^\circ - \tan^{-1} V_t(r)/V_0(r)$ . Note that the effect of  $\alpha_a$  were not considered in the previous preliminary study<sup>5</sup>.

Equation (1) reveals that the thrust produced by the propeller is a function of Blade number ( $B$ ), tip Mach number ( $M_t = \frac{V_t(R_t)}{c_0}$ ), lift and drag coefficients ( $C_L, C_D$ ), and chord of the propeller ( $c$ ),  $T = f(B, M_t, c, C_L, C_D)$ . This paper will focus on the noise variation with tip Mach number ( $M_t$ ) and Blade number ( $B$ ) while keeping thrust and blade solidity as constant. The effects on noise due to blade geometry will be

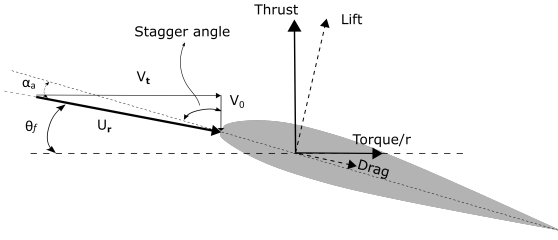


**Figure 2.** Blade airfoil section.

discussed in the subsequent sections titled “Effects on the balance between tonal and broadband noise due to airfoil geometry”. The blade solidity ( $\sigma$ ) is defined as,

$$\sigma = \frac{c}{P_c} \quad (2)$$

where  $P_c(r) = 2\pi r/B$  is the local blade pitch. Substituting this expression of  $P_c(r)$  into that for  $\sigma$  in equation (2), and for a fixed diameter of the propeller, to maintain blade solidity constant, it yields,

$$\sigma = \text{Constant} \rightarrow Bc = \text{Constant} \quad (3)$$

Hence, to maintain constant blade solidity, the product  $Bc$  was kept constant while changing the blade number<sup>29</sup>. As the ATR42 blade profiles were not available, the blade chord distribution  $c(r)$  along the span was assumed to be identical to that of the distribution given in<sup>9</sup>, but scaled by a factor chosen to provide the required thrust. Note also that sweep and lean were not considered in this study. This procedure is described in the flow chart shown in Fig. 3, indicated by the red arrows.

The predicted variation in noise with  $B$  and  $M_t$  will be undertaken relative to the baseline ATR42 takeoff case, whose parameters are listed in Table 1 and whose power requirement is 2160 shp<sup>7,8</sup>. We further assume that the propulsive efficiency at takeoff is 85%, resulting in a thrust requirement of 22.82 kN at a take-off speed of 112 kts.

**Table 1.** Baseline case parameters considered for the study

Propeller Diameter ( $D_t$ )	3.96 m
Blade number ( $B$ )	6
Speed (RPM)	1050
Aircraft Mach number ( $M_x$ )	0.17
Thrust (kN)	22.82

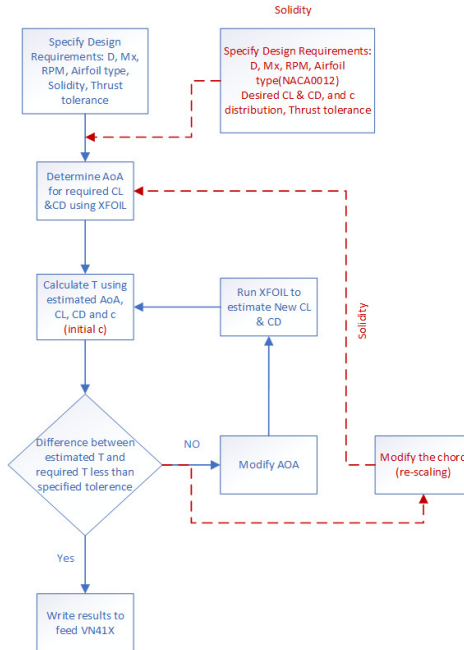


**Figure 3.** Flowchart for estimating blade solidity (highlighted with red-colour dotted path) for baseline case at constant thrust, and  $\alpha_a$  (blue-colour solid path) distribution for constant thrust and solidity at specified airfoil geometry, tip Mach, number of blades.

### Iterative method for the calculation of spanwise lift and drag distribution

This section describes an iterative method for calculating the radial variation in lift and drag spanwise distributions for a particular combination of blade number  $B$  and tip Mach number  $M_t$ . This information will be required to perform the parametric study described in this paper. At each spanwise position the angle of attack  $\alpha_a(r)$ ,  $C_L$  and  $C_D$  was computed using the iterative method described in Fig. 3 based on predictions of the

blade solidity, thrust, tip speed and axial flow speed. The method essentially involves iteratively updating the estimate for  $\alpha_a(r)$  until successive estimates for the total thrust are within some specified tolerance. The panel code XFOIL was used to estimate the local lift and drag coefficients. Full details of the iterative method are provided in the flow chart in Fig. 3. In the parametric study the blade number  $B$  was varied between 4 and 16 and the tip Mach number  $M_t$  was varied between 0.42 and 0.77 around a baseline case of  $B = 6$  and  $M_t = 0.53$  while the propeller diameter was kept constant.

### Results of the iterative method for baseline geometries

Predictions obtained using the iterative method are presented in Fig.4 and Fig. 5 for the three baseline airfoil geometries of NACA0012, NACA4312 and NACA6312. Figure 4a shows the radial chord distribution used in all cases while Fig.4b indicates the radial distribution of the lift-to-drag ratios, designed to have the same thrust distribution, as evident in Fig. 5a. The variation in  $\alpha_a(r)$  necessary to achieve this match in distribution is shown in Fig. 5b.

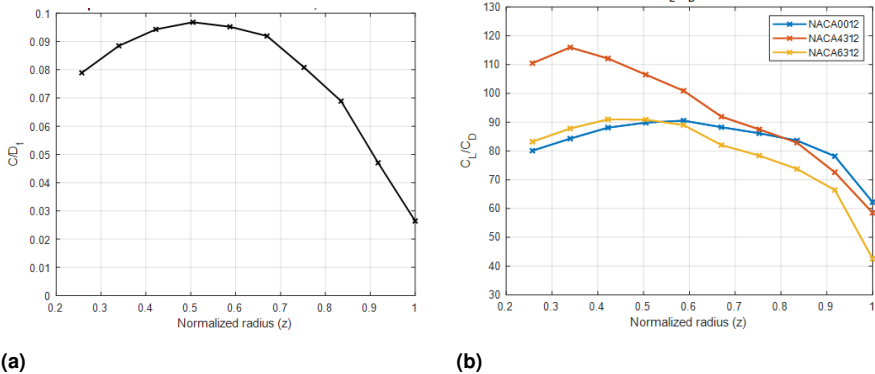


**Figure 4.** Span-wise distribution of (a) chord (b) ratio  $C_L/C_D$  for baseline case.

The NACA4312 profile has the highest lift-to-drag ratio compared to the other airfoils, which is one of the desired parameters for aerodynamic performance. Figure 5 shows the

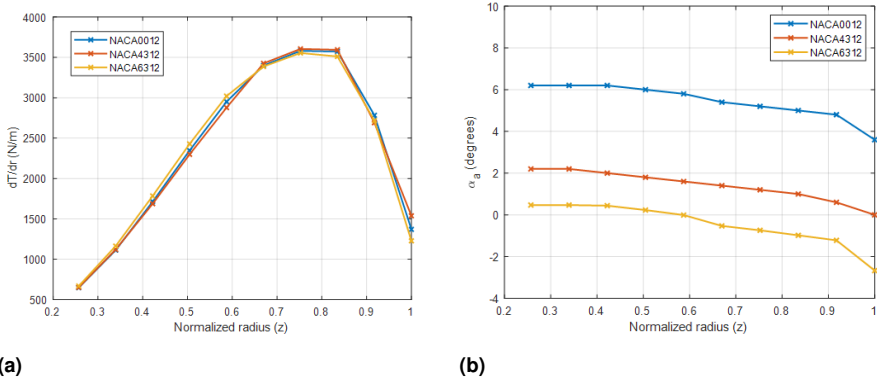


**Figure 5.** Span-wise distribution of (a) thrust per unit span for baseline case (b) local angle of attack/incidence  $\alpha_a(r)$ .

spanwise distribution of  $\alpha_a(r)$  and thrust for the different airfoils under consideration. The maximum thrust is obtained at 83 % of the propeller radius, which is consistent with the general propeller characteristics presented in<sup>30</sup>. The symmetric NACA0012 airfoil can be observed to have the highest angle of attack  $\alpha_a(r)$  compared to the cambered airfoils, which could have been anticipated since the cambered airfoils are intended to produce higher lift at lower  $\alpha_a(r)$  when compared to the symmetric airfoil.

### Acoustic calculations

Propellers radiate both tonal and broadband noise. Tones occur at harmonics of the blade passing frequencies (BPF) resulting from periodic time variations in the blade loading relative to the stationary observer. Broadband noise has a broad frequency spectrum and is predominantly caused by the turbulent boundary layer passing over the propeller blade trailing edges. The main aim of this paper is to apply existing analytic and semi-analytic noise prediction methods to investigate the balance between tonal and broadband noise with respect to its frequency spectrum and directivity for an arbitrary propeller configuration. We start by providing an overview of the prediction

---

methodology, with emphasis on highlighting the similarities between the tonal and broadband noise formulations.

### *Tonal Noise*

For isolated propellers, the overall tonal noise has two main components at subsonic propeller tip speeds: loading and thickness noise. The propeller blades experience a mean loading distribution that is steady in the propeller's frame of reference but is periodically varying with respect to a stationary observer. This mechanism is generally referred to as 'loading noise' and is of dipole in nature. The finite thickness of the propeller blade displaces the air and is therefore of monopole in nature, and is referred to as 'thickness noise'.

At low tip speeds, loading noise is the dominant noise source while at higher tip speeds, thickness noise becomes more important<sup>11</sup>. At even higher tip speeds, where the blade tip becomes transonic, a third source, namely quadrupole noise, can contribute significantly to the total. However, our parametric study will be restricted to purely subsonic tip speeds so that quadrupole noise can be neglected<sup>31</sup>. In this parametric study we adopt the tonal noise formulation developed by Parry<sup>3</sup>. The model uses predictions of the steady lift and drag coefficients across the chord and span, which is integrated over the blade surface, which is approximated as a flat plate.

### *Broadband noise*

Broadband self-noise of the propeller is predominantly produced by the interaction of the turbulence boundary layer with the propeller blade trailing edge. In this study, broadband self-noise is predicted using the formulation due to Blandeau<sup>4</sup> which uses strip theory to account for the spanwise variation of aerodynamic and geometric quantities. This semi-empirical formulation makes use of the isolated flat plate airfoil response function due to Amiet<sup>25,26</sup> which was further extended by Roger and Moreau<sup>32</sup>

to include oblique gusts. Computation of the far-field acoustic pressure Power Spectral Density (PSD) are based on estimates of the boundary layer PSD ( $\Phi_{pp}$ ) on the blade surface close to the trailing edge, which is estimated here using the semi-empirical model by Rozenberg<sup>27,33</sup>.

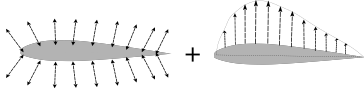
Further, irrespective of airfoil geometry, the span-wise correlation length was estimated by setting empirical constant  $\zeta_2 = 1.6$  observed by Brooks and Hodgson<sup>21</sup> for NACA0012 airfoil at zero angles of attack. This is one of the simplifying assumptions that has been used in the current study. More details about the relation between  $\zeta_2$  and span-wise correlation length are given in Appendix . The panel method code XFOIL<sup>6</sup> was used to determine the boundary parameters near the trailing edge, which serves as input to the  $\Phi_{pp}$  model. Finally, the far-field noise is predicted using a methodology similar to Kim and George<sup>19</sup>, with source non-compactness along the chord now included.

### *Summary of the tonal and broadband prediction models*

The mechanisms of tonal and broadband noise radiation from subsonic propellers share many common features, with the significant difference that tonal noise arises from periodic events while broadband noise is essentially a stochastic process. Unsurprisingly, therefore, the tonal and broadband noise formulations share many common similar terms, which we highlight below in Table 2. Terms in the tonal and broadband formulations, listed on the table's left and right, are highlighted in either blue or red to indicate source terms and radiation terms respectively. Details of the tonal and broadband noise model may be found in the Appendix. Here, we discuss only the main features of the model, highlighting the similarities and differences between the tonal and broadband formulations.

The expressions for tonal and broadband noise in Table 2 are in the form of a summation of acoustic modal components. This table indicates that tonal noise can be predicted by an integration of the source term across the span while broadband

**Table 2.** Comparison between tonal and broadband noise formulations

	Tonal	Broadband
	 Monopole (thickness) + Loading (Dipole)	 Dipole
SPL	$\text{SPL}_T(r_0, \theta, \omega) = 10 \log_{10} \left( \frac{\overline{P}_m^2(r_0, \theta, \omega)}{P_{\text{ref}}^2} \right)$ <p><math>\overline{P}_m^2</math> is the mean square sound pressure at the <math>m^{\text{th}}</math> harmonic of blade passing frequency.</p>	$\text{SPL}_B(r_0, \theta, \omega) = 10 \log_{10} \left( \frac{2 b_w S S_{pp}^{TE}(r_0, \theta, \omega)}{P_{\text{ref}}^2} \right)$ <p><math>b_w</math> = bandwidth for 1/3<sup>rd</sup> octave <math>0.232 \times 2\pi \times f</math>  <math>S S_{pp}^{TE}</math> = far-field power spectral density</p>
Acoustic pressure/power spectral density	$\overline{P}_m^2(r_0, \theta, \omega) = \left[ \frac{B R_t}{2\pi r_o (1 - M_x \cos \theta)} \right]^2$ $\times \int_{r_h}^{R_t} \left\{ [S_T(r) D_{\nu T}(r)]^2 + [S_L(r) D_{\nu L}(r) + S_D(r) D_{\nu D}(r)]^2 \right\} dr$ <p><math>k_m = \frac{\omega_m}{c_0(1 - M_x \cos \theta)}</math> takes discrete values at BPF.</p>	$\text{Total } S S_{pp}^{TE} = \sum_j S S_{pp,j}^{TE}$ $S S_{pp,j}^{TE}(r_0, \theta, \omega) = \frac{\pi}{2B} \left( \frac{c_j}{R_t} \right)^2 \left[ \frac{B R_t}{2\pi r_o (1 - M_x \cos \theta)} \right]^2$ $\times \sum_{\nu=-\infty}^{\infty} \left[ S_{BB}(\bar{r}_j) \times \int_{r_j - \Delta r_2}^{r_j + \Delta r_2} D_{\nu BB}(r) dr \right]^2$ <p><math>j</math> = number of strips; <math>k_0 = \frac{\omega}{c_0(1 - M_x \cos \theta)}</math> takes continuous values.</p>
Mode order	$\nu = mB$ , and $\omega_m = mB\Omega$	$\nu = \text{integer}$
Source	$S_T(r, \omega_m) = i\rho c_0 b U_r \Psi_V$ $S_L(r, \alpha, \omega_m) = \frac{dL}{dr} = \frac{1}{2} \rho U_r^2 C_L \int_{-\frac{\pi}{2}}^{\frac{\pi}{2}} e^{i k_x X} F(X) dX$ $S_D(r, \alpha) = \frac{dD}{dr} = \frac{1}{2} \rho U_r^2 c C_D$	$S_{BB}(\bar{r}_j) =  \mathcal{L}^{TE}(k_r, K_{X,\nu}, \kappa_\nu) _{\kappa_\nu=0} \sqrt{S S_{qq}(0, K_{X,\nu})}$ $S S_{qq}(k_r = 0, K_{X,\nu}) = \frac{1}{\pi} l_r (K_{X,\nu} U_c, k_r) \Phi_{pp}(K_{X,\nu}, U_c)$ $\mathcal{L}^{TE}(k_r = 0, K_{X,\nu}, \kappa_\nu) = \frac{1}{c_j/2} \times \int_{-c_j/2}^{c_j/2} g^{TE}(X, k_r, K_{X,\nu}, M_{r_j}) e^{i\kappa_\nu(X+c_j/2)} dX$
Radiation	$D_{\nu T}(\theta, \omega_m) = k_m J_\nu(k_m r \sin \theta)$ $D_{\nu L}(\theta, \alpha, \omega_m) = i(k_m \cos \theta \sin \alpha + \frac{1}{r} \nu \cos \alpha) J_\nu(k_m r \sin \theta)$ $D_{\nu D}(\theta, \alpha, \omega_m) = i(k_m \cos \theta \cos \alpha - \frac{1}{r} \nu \sin \alpha) J_\nu(k_m r \sin \theta)$	$D_{\nu BB}(\theta, \alpha, \omega) = (k_0 \cos \theta \sin \alpha + \frac{1}{r} \nu \cos \alpha) J_\nu(k_0 r \sin \theta)$

noise is computed by summing the source contributions from a number of 'strips', which are assumed to be larger than the boundary layer turbulence integral length-scale. However, the most significant difference between the tonal and broadband formulations is the range of possible acoustic mode orders  $\nu$  that can be excited. In the case of

tonal noise generation, only a single acoustic mode order  $\nu$  is generated at each blade passing frequency  $\omega = m\Omega$ . By contrast, broadband noise will excite all possible modal  $\nu$  orders,  $[-\infty, \infty]$ , although in practice their range is limited by their relative radiation efficiencies. This paper will demonstrate that this difference in the number of modes is the main cause of the variation in the characteristics of the noise due to changes in blade number and tip speed. In addition to the number and range of acoustic modes excited by the tonal and broadband sources there are other significant but less important differences, which we now discuss. Predictions of the far-field tonal noise obtained using the theory summarised in Table 2 are estimated by integrating the source and radiation terms along the span. However, predictions of broadband noise are made using strip theory where the far-field pressure PSD is given by the sum of individual PSDs over a finite number of strips along the span.

The propeller tone predictions presented in this paper are assumed to originate from the three sources; thickness noise, loading noise and the noise due to drag, whose source terms are referred to here as  $S_T(r)$ ,  $S_L(r)$ , and  $S_D(r)$  respectively. More details about these source terms and their respective radiation terms are summarised in Table 2 and in Appendix. By contrast, broadband noise is assumed to originate from a single mechanism involving boundary layer interaction with the trailing edge.

The formulations presented in Table 2 were used to predict the tonal noise at the BPF and the broadband noise spectra up to the frequency of  $f = 12.5$  kHz. Assuming axisymmetry of the radiated noise, the sound power radiated by the rotor was computed from,

$$W(f) = 2\pi r_0^2 \sum_n \frac{\overline{p^2}(\theta_n, f)}{\rho c} \sin \theta_n \Delta \theta_n \quad (4)$$

where  $\overline{p^2}(\theta_n, f)$  is the mean square pressure tonal amplitude  $P_m^2$  for tones or the PSD  $SS_{pp}$  for broadband noise calculations as given in Table 2,  $r_0$  is the radius of the surface

of integration and  $\theta_n$  are the discrete prediction angles and  $\Delta\theta_n$  is the angle between successive prediction angles. Finally, the Sound Power Level PWL is estimated from,

$$\text{PWL}(f) = 10 \log_{10} \left( \frac{W(f)}{10^{-12}} \right) \quad (5)$$

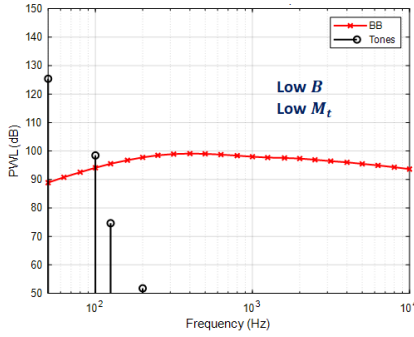
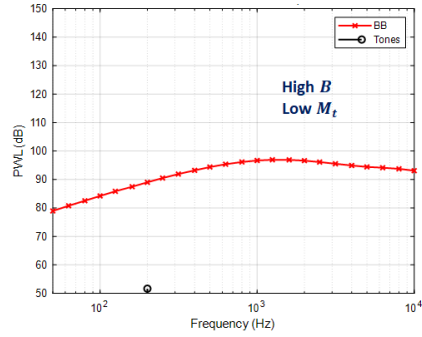
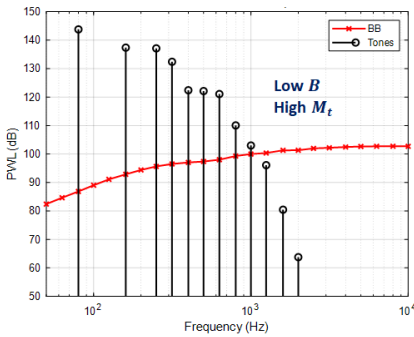
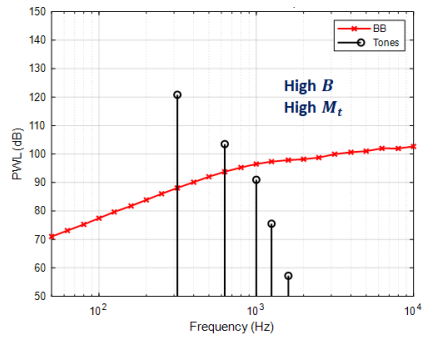
Note that all spectral predictions in this paper are presented in  $1/3^{\text{rd}}$  octave frequency bands while Overall Acoustic Sound Power Levels, OSWL, are calculated by integrating the spectra over the frequency range of 50Hz-12.5kHz.

## Results for NACA0012 airfoil

Before investigating the effect of airfoil geometry on propeller noise we first apply the formulations presented in Table 2 to investigate the variation in tonal and broadband noise with variations in tip Mach number between  $0.42 < M_t < 0.77$  and blade number  $B$  between 4 and 16 for a propeller with symmetric NACA0012 blade profiles with 1.98 m span and 1.6 mm trailing edge thickness whose chord profile is given in Fig. 4a. In this parametric study, the propeller blade solidity and thrust were kept constant by re-scaling the chord or/and estimated new lift and drag coefficients using XFOIL using the procedure discussed in Section .

### Sound Power Level (PWL) spectra

We first compare in Fig. 6 the tonal and broadband Sound Power Level spectra for all four extreme combinations of  $B = 4$  and  $B = 16$ , and  $M_t = 0.42$  and  $M_t = 0.77$ . As is well understood from the classical work of Gutin<sup>13</sup>, the tonal amplitudes can be observed to decay rapidly with increasing harmonic of BPF, while the broadband noise spectrum is broadly 'flat', except at high tip speeds where it can be observed to slowly increase. The most important aspect of these results is that the balance between tonal and broadband contributions is highly sensitive to the combination of  $M_t$  and  $B$ .

(a)  $B = 4, M_t = 0.42$ (b)  $B = 16, M_t = 0.42$ (c)  $B = 4, M_t = 0.77$ (d)  $B = 16, M_t = 0.77$ 

**Figure 6.** PWL against frequency for extreme tip Mach numbers and blade numbers for NACA0012

### Tonal Noise

The tonal amplitudes at harmonics of BPF are highest when  $B$  is smallest and  $M_t$  is greatest. This combination of parameters provides the highest level of tonal noise. By contrast, the tonal amplitudes are negligible compared with broadband levels when the blade count is high and the speed of rotation is relatively low. In comparison, the shape of the broadband spectrum and level appears to be relatively insensitive to variations in  $B$  and  $M_t$  compared to the tonal spectrum.

The decay of the tonal amplitudes with increasing frequency shown in Fig. 6 approximately follows an exponential decay with frequency. This behaviour can be

attributed to the fact that, at a single BPF harmonic  $m$ , only a single acoustic mode  $\nu_T = mB$  is excited whose radiation efficiency, as determined by the Bessel function term  $J_\nu$  in Table 2<sup>34</sup>. Recently, at the AIAA 2022 keynote presentation by Roger, and in one of their conference articles, Acevedo Giraldo et al.<sup>35</sup> have shown that the Bessel function rapidly drops to zero as its order exceeds the value of its argument in absolute terms. Therefore, at higher acoustic mode orders ( $\nu_T$ ), the radiation efficiency of the propeller drops. As discussed by Parry and Crighton<sup>36</sup>, the asymptotic behaviour of the Bessel function decays exponentially with increasing  $\nu = \nu_T = mB$  such that for large  $m$ ,  $J_\nu$  can be approximated by  $J_\nu(mB \operatorname{sech}\beta) \sim \frac{\exp[mB(\tan\beta - \beta)]}{(2\pi mB \tan\beta)^{1/2}}$ , where  $\operatorname{sech}\beta = \frac{zM_t \sin\theta}{(1 - M_x \cos\theta)}$ .

Another important feature of the results in Fig. 6a and 6c is that, at a fixed blade number, tonal amplitudes increase markedly with  $M_t$ . This dramatic increase is due to a combination of increased blade loading  $S_L(r)$ , which is proportional to  $M_t^2$ , but mostly due to increases in the radiation efficiency of their acoustic modes. We note that thickness noise can generally be neglected at these subsonic tip speeds.

### Broadband Noise

By contrast to the behaviour of the discrete tonal spectrum, broadband noise in each narrow frequency band excites a wide range of acoustic modes  $\nu = n$ , where  $n$  takes all integer values. The overall efficiency of the broadband noise therefore, is governed by the efficiency of the most efficient modes. Whilst the tonal noise spectrum in Fig. 6 decays sharply with increasing frequency due to its dependence on single acoustic modes, the broadband noise spectrum is much 'flatter' since, in principle, it comprises all acoustic modes  $\nu_{BB} = [-\infty, \infty]$  with varying radiation efficiencies included in the directivity term  $D_{\nu_{BB}}$ .

Figure 6 indicates that the spectral shape of the broadband noise is sensitive to the combination of  $B$  and  $M_t$ . The low frequency content of the broadband noise spectrum

can be observed to reduce with increasing  $B$  and  $M_t$  while high frequencies tend to increase. The reason for this behaviour can be explained by the dependence on the form of the surface pressure spectrum  $\Phi_{pp}$  on the dimensionless frequency  $\tilde{\omega}$  appearing in surface pressure spectrum source term Eq. 29 in the Appendix, where  $\delta$  is the boundary layer thickness at the trailing edge and  $u_t$  is the friction velocity estimated from the wall shear stress, Hwang<sup>37</sup>.

The dimensionless frequency  $\tilde{\omega}$  determines the low and mid frequency part of the frequency spectrum  $\tilde{\omega} = \omega\delta/u_t < 100$ , which is mostly governed by the outer-scales of the boundary layer, which is controlled by the boundary layer thickness  $\delta$ . The high-frequency part of the spectrum, which from Eq. 29 occurs when  $\tilde{\omega} = \omega\eta/u_t^2 > 0.3$ , is controlled by inner scales of turbulence. We note that these two frequency regions exhibit different scaling laws  $\tilde{\omega}^n$ , where  $n = 2$  at low frequencies,  $n = -1$  in the overlap transition region and between  $n = -1$  and  $-5$  at high frequencies.

Therefore, the reason the broadband noise spectrum reduces at low frequencies and increases at high frequencies as  $B$  and  $M_t$  increases is due to a reduction in the non-dimensional frequency  $\tilde{\omega}$ . This behaviour is predominantly due to the reduction in the boundary thickness  $\delta$ , which is known to reduce with increasing flow speed and reduce with increasing  $B$  due to a reduction in the chord necessary to maintain constant solidity. In conclusion, therefore, the broadband spectra depend on both the blade chord but also the tip Mach number which also affects the angle of attack.

### *Modal breakdown*

According to the theoretical expressions in Table 2 the main difference between the two formulations for the tonal and broadband noise is number of azimuthal acoustic mode orders  $\nu$  that can be excited. For tones, at each blade passing frequency of order  $m$ , only a single acoustic mode is excited  $\nu_T = mB$ , while for broadband noise  $\nu_{BB}$  can take

all possible integer values (... -2, -1, 0, 1, 2, 3 ...) up to some maximum value, which according to the form of the Bessel function appearing in the directivity term is in the range given by,

$$\nu \leq k_0 r \sin \theta \tag{6}$$

By way of example, Fig. 7a shows the modal distribution of broadband and tonal SPL versus  $\nu$  for the baseline case with  $B = 6$  and  $M_t = 0.62$  at a polar angle of  $90^\circ$ . We note that these modal distributions are a result of the combination of source terms and their respective radiation terms. However, the dominant behaviour in these modal spectra can be explained by the different number of acoustic modes and their individual behaviours.

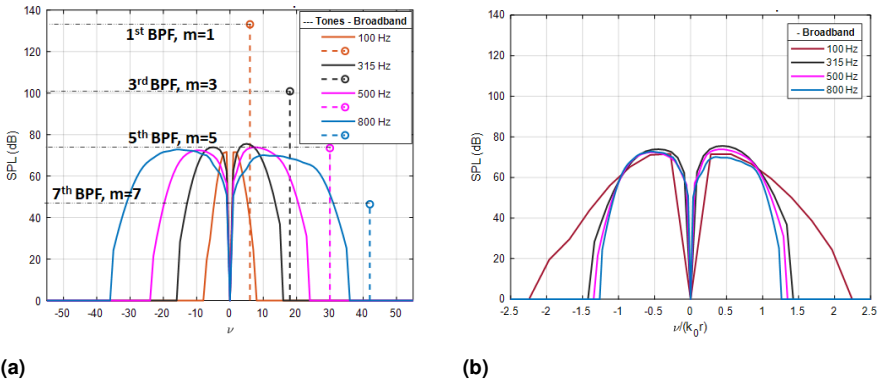


**Figure 7.** (a) Tonal and broadband SPL against mode order  $\nu$  (b) Modal Broadband SPL against  $\nu/(K_0 r)$

To aid readability, the tonal mode distributions are only presented at the odd harmonic tonal frequencies while the broadband distributions are plotted at the same center frequencies but in 1/3 octave bands. It can be observed that the broadband modal SPL distribution is symmetric around  $\nu = 0$  since it can take both positive and negative values. By contrast only a single positive azimuthal mode order is present for the tones at each harmonic of BPF.

Consistent with the frequency spectrum in Fig. 6 the tonal modal amplitudes decay exponentially with increasing  $m$  (and hence  $\nu$ ). By contrast the broadband distribution at each center frequency take a broad range of values over a well defined range of  $\nu$ . Note that there is no contribution to the radiation from  $\nu = 0$ , which is due to the factor  $(k_0 \cos \theta \sin \alpha + \nu/r \cos \alpha)$  appearing in the expression for the broadband directivity. Physically, the weak radiation of the  $\nu = 0$  mode can be explained by the inability of the spatial variation in unsteady blade loading around the propeller disc to couple into this axi-symmetric mode, which is constant around the propeller disc.

The mode distribution plot in Fig. 7 explains clearly why the broadband noise spectrum is relatively 'flat' while the tonal amplitudes decay sharply with increasing frequency since, at each frequency, overall noise is the sum of mean square pressures over acoustic mode orders  $\nu$ . In this example, the broadband noise spectrum over the range of frequencies shown (between 100Hz and 800Hz) will increase with increasing frequency as the number of modes increases, while the level remains roughly the same. At higher frequencies, however, while the range of modes continues to increase the mean square pressure in each mode will decay with increasing frequency due to the decay of the source term  $S_{qq}(\omega)$  appearing in Table 2.

In order to illustrate the universality of the mode distribution for broadband noise, its mode distribution plotted in Fig. 7a for  $\theta = 90^\circ$  is plotted again in Fig. 7b against  $\nu/k_0 R_t$ . Apart from the lowest frequency of 100Hz, where comparatively few modes are excited, the mode distribution closely collapses on  $\nu/k_0 R_t$ , suggesting that over a narrow frequency range (700Hz in this case) the mode distributions are roughly frequency independent. At this radiation angle, therefore, most of the noise is radiated by the modes in the range  $-k_0 R_t < \nu < k_0 R_t$  whose amplitudes decay rapidly at values of  $\nu$  outside of this range. The form of the Bessel function terms appearing in Table 2 for the directivity suggest that acoustic modes for which  $\nu > k_0 R_t \sin \theta$  are cutoff and do not

radiate, as observed in Fig. 7. It is interesting to observe that the modes with maximum mean square pressure have mode order  $\nu \sim k_0 R_t / 2$ . Note that a wide range of acoustic modes are excited at lower radiation angles  $\theta$  owing to the form of the Bessel function, as discussed by Blandeau<sup>4</sup>.

### *Overall Sound Pressure Level (OASPL) directivities*

We now compare in Fig.8 the directivities of far field radiation of the overall tonal and broadband SPL with polar angle for the four combinations of  $B = 4$  and 16 and  $M_t = 0.42$  and 0.77 discussed above. We note that the tonal and broadband directivities have fundamentally different behaviour. Tonal noise can be observed to have peak values near the plane of rotation. By contrast the broadband directivity has peak values on-axis both upstream and downstream and has minimum level in the plane of rotation. The reasons for this different behaviour is again due to the number of acoustic modes that are able to be excited by tonal and broadband noise mechanisms. The directivity characteristics of tonal and broadband noise are now discussed in detail below.

#### 1. Tonal Noise:

The theoretical expression for the far field tonal noise in Table 2 indicates that only a single acoustic mode of order  $\nu = mB$  is excited at each harmonic  $m$  of the blade passing frequency. According to this expression the directivity due to loading noise is determined by the term  $(k_m \cos \theta \sin \alpha + \frac{1}{r} \nu \cos \alpha) J_\nu(k_m r \sin \theta)$ . Peak radiation is therefore predicted at the polar angle  $\theta_{pk}$  corresponding to when  $(kr \sin \theta_{pk}) \sim (\nu + 1)$ , which Fig.8 suggests is close to the plane of rotation. In addition, 'flyover' effects due to the term  $(1 - M_x \cos(\theta))^{-1}$  cause an additional shift in peak radiation angle towards the forward arc.

#### 2. Broadband Noise:

The main difference between the theoretical expression in Table 2 for the radiation due

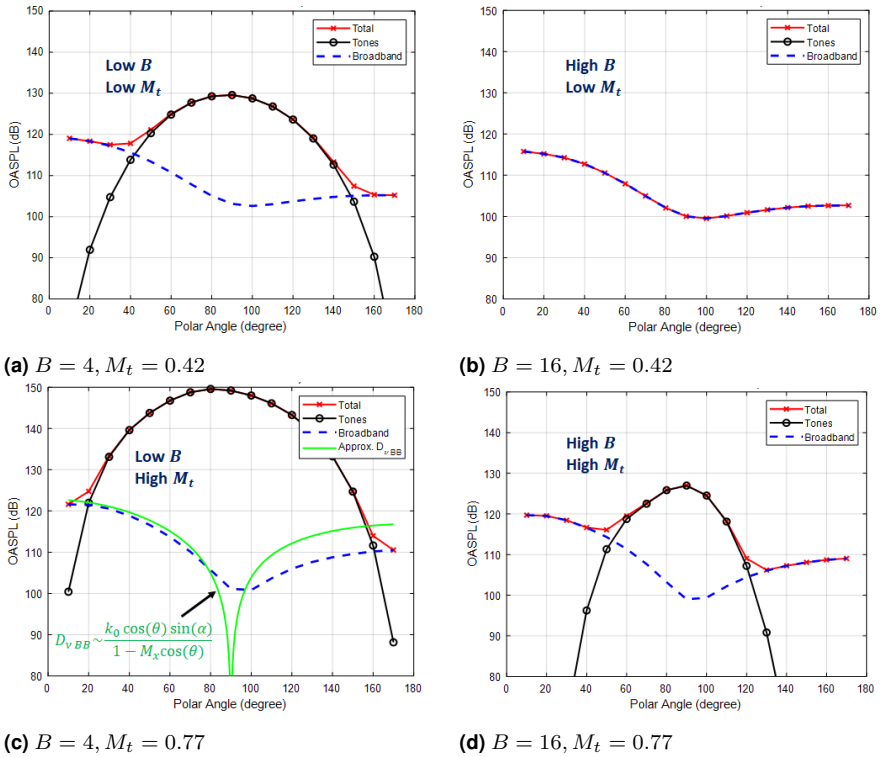


**Figure 8.** Individual source OASPL directivities for NACA0012 at tip Mach ( $M_t$ )= 0.42 and blade numbers of (a)  $B= 4$  (b)  $B= 8$  (c)  $B= 12$  (d)  $B= 16$

to propeller broadband self-noise and the tones is that, in a narrow frequency band, broadband noise contains a potentially large number of incoherent acoustic modes of order  $\nu$ . The directivity for broadband noise in a narrow frequency band can be seen to be of the form  $\sum (k_0 \cos\theta \sin\alpha + \frac{1}{r} \nu \cos\alpha) J_\nu(k_0 r \sin\theta)$ . We note that the Bessel function terms  $J_m^2(k_0 r \sin\theta)$  oscillate much faster with  $\theta$  than the terms  $(k_0 \cos\theta \sin\alpha + \frac{1}{r} \nu \cos\alpha)$ . We also note the Bessel function identity,

$$1 = J_0^2(x) + \sum_{\nu=-\infty}^{\infty} J_\nu^2(x) \tag{7}$$

When all acoustic modes of order  $\nu$  are summed incoherently, therefore, the contribution to the directivity due to the Bessel function terms becomes relatively small and the broadband directivity  $D_{\nu BB}$  becomes principally governed by the terms  $(k_0 \cos \theta \sin \alpha + \nu/r \cos \alpha)$ , which may be interpreted as the directivity that would occur due to a single dipole source radiating into free field.

We have shown that the acoustic modes with relatively low mode order  $\nu \sim k_0 R_t/2$  contribute most to the overall far field noise (Fig. 7). The contribution to the radiation from the second term in  $(k_0 \cos \theta \sin \alpha + \frac{1}{r} \nu \cos \alpha)$  is therefore relatively small and can be neglected and hence the far field directivity is roughly of the form,

$$D_{\nu BB} \sim k_0 \cos \theta \sin \alpha \quad (8)$$

whose peak radiation occurs on axis at  $\theta = 0$  and  $\pi$ , consistent with the predictions in Fig. 8. Equation 8 is plotted in Fig. 8c whose level has been adjusted to give best fit to the predicted broadband forward-arc directivity. Note also that the additional factor of  $(1 - M_x \cos(\theta))^{-1}$  has been included to take into account 'flyover' effects. This simple function is seen to capture the general shape of the predicted broadband directivity, except at angles in the rearward direction  $\theta \sim \pi/2$ . The small discrepancy between the predicted and approximate directivities is most likely due to source effects omitted from this simple analysis.

### 3. Interpretation:

Previous sections have highlighted the important differences between the directivities and dependence on propeller tip speed between tonal and broadband self-noise. We have demonstrated that these differences arise solely due to the number of acoustic modes which can be excited. In the case of tones, only a single acoustic mode is excited at each blade passing frequency while a potentially much larger number of acoustic modes can be excited for the broadband noise in a narrow frequency band.

Another interpretation of this difference arises from the coherence between the unsteady blade loading between the tones and broadband noise. The directivity due to tonal noise is the result of integrating the mean loading contributions from  $B$  identical blades around the propeller disc whose subsequent radiation, therefore, has the form of a single Bessel function of order  $\nu$ . By contrast, the broadband noise directivity is the result of integrating  $B$  incoherent unsteady source distributions whose subsequent radiation is therefore identical to that due to  $B$  single blades radiating in isolation of each other. Since the blade-to-blade periodicity is now absent in the broadband case, there is no Bessel function dependence and peak radiation occurs close to the axis of rotation, i.e., away from the plane of rotation. This fundamental difference in behaviour in radiation between tones and broadband noise discussed above has been observed experimentally by Gojon et al.<sup>23</sup> on a small low-speed propeller rig of APC 9x6 SF, APC 11x4.7 SF, and ISAE 2 at higher tip speeds. [More recently, Baskaran et al.<sup>38</sup> also have observed a similar trend in tonal and broadband noise with a change in blade numbers.](#) The broadband noise was observed to be maximum at angles away from the plane of rotation and a minimum near the plane of rotation.

#### *Overall Acoustic Sound Power Level (OSWL)*

In this section we investigate the variation in overall tonal and broadband Sound Power Level OSWL with blade tip Mach number  $M_t$  for the propeller comprising NACA0012 blades. Overall broadband noise was obtained by integrating its frequency spectrum over the frequency range of 50 Hz - 12.5 kHz and polar emission angles between  $10^0 - 170^0$ . The results are shown in Figure 9 for blade numbers  $B = 4, 8, 12$  and 16 for tip Mach numbers in the range between 0.4 and 0.8. We note that the tonal sound power exhibits a much greater variation of more than 70dB at low  $M_t$  than the broadband sound power, which varies by less than 3dB. The variation in broadband power is therefore plotted separately in Fig. 9b on a smaller scale to make clear the dependence

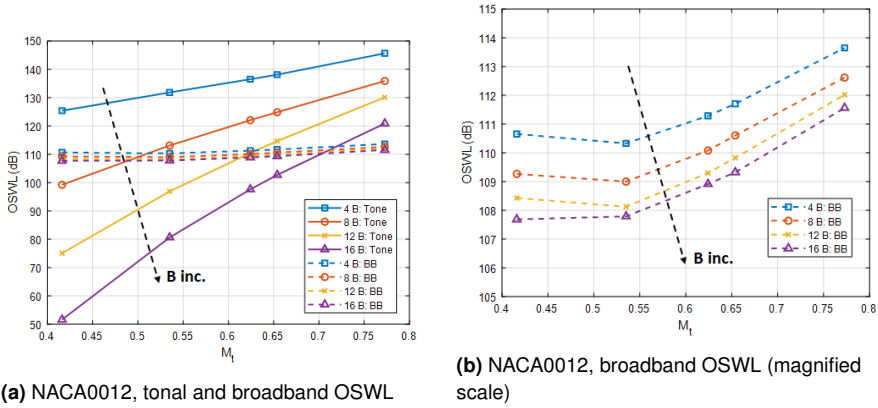


**Figure 9.** Tonal and Broadband OSWL against tip speed at different blade numbers for NACA0012 airfoil geometry

of the sensitivity of the broadband levels to  $B$  and  $M_t$  when the solidity and thrust is maintained constant.

We note from Fig. 9a that the tonal overall sound power level is much more sensitive to  $B$  at the lower tip speeds. By contrast the broadband OSWL variation with  $B$  remains roughly independent of  $M_t$  with variations of no more than approximately 3dB. The very large variation of the tonal amplitudes with  $M_t$  and  $B$  is almost completely governed by the variation in radiation efficiency of their respective modes, with the contribution from the increased steady loading due to increasing  $M_t$  and reducing  $B$  being much smaller. The contribution of the change in noise due to the steady blade loading can be estimated by noting that it is proportional to  $M_t^2$  and inversely proportional to  $B$  (to maintain constant thrust). This dependence corresponds to changes in noise of just 6dB due to a doubling of  $M_t$  and an increase in noise of 6dB due to the reduction in  $B$  by a factor of 4 considered in this paper.

We note that the variation in broadband OSWL is not proportional to  $B$  as might be expected for propellers with  $B$  identical blades since the blade chord has been reduced while increasing  $B$  to maintain constant solidity since  $Bc = constant$ . The boundary

layer thickness at the trailing is therefore thinner as  $B$  is increased, leading to a reduced boundary layer pressure spectrum, which drives the broadband noise radiated to the far field. This phenomenon has been reported in detail by the authors in a previous conference paper<sup>5</sup>.

One of the most important aspects of Fig. 9a is the existence of a critical tip Mach number at which the tonal and broadband levels are identical. The broadband levels in Fig. 9a therefore appear to provide a lower limit noise 'floor' below which it may not be possible to achieve further noise reductions by reducing tip speed and blade number without specifically targeting the broadband noise. This critical tip Mach number can be observed to shift to higher tip Mach numbers as the blade number increases. The effect on the broadband OSWL due to changes in airfoil geometry will be investigated in Section titled "[Effects on the balance between tonal and broadband noise due to airfoil geometry](#)".

#### *Overview of parametric study for NACA0012 blades*

The noise predictions presented in the previous section are now summarised in the colour maps shown in Fig.10 in which the OSWL is shown versus  $M_t$  and  $B$  for the tonal, broadband, and when summed together. The colour map of total noise shows a clear distinction between the regions dominated by tonal and broadband noise, with the two regions separated by the critical tip Mach number which increases with increasing  $B$ . The two regions where overall tonal noise is greater than 10dB above the broadband noise, and vice-versa, are indicated in the Fig.10. As shown previously, the Fig.10a indicates that overall broadband noise is the dominant noise source in the right-hand lower part of the colormap, corresponding to higher blade number and lower tip Mach number, while tonal noise is dominant at lower blade number and higher tip Mach numbers. These results provide general guidelines on low-noise propeller design. However, we note that the precise balance between tones and broadband noise will vary in detail for different

blade geometries. Moreover, other sources of tonal and broadband noise may also be presented, particularly for installed propellers which operate in a turbulent environment or when there is a strong tip vortex. The sensitivity of the balance of tonal and broadband noise due to variations in blade geometry will be investigated in the next section.

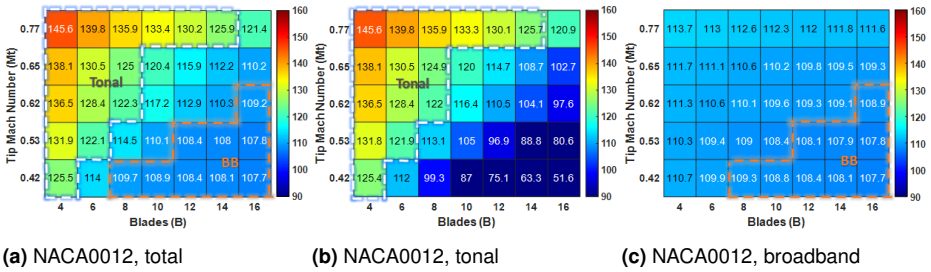


**Figure 10.** 2D plot representation of OSWL for NACA0012 airfoil geometry for tip Mach and blade number (a) total (b) tonal (c) broadband.

## Effects on the balance between tonal and broadband noise due to airfoil geometry

This section investigates the effect of airfoil geometry on the balance between tonal and broadband noise radiation over a range of blade number  $B$  and tip Mach number  $M_t$ . All previous studies presented above relate to the symmetric NACA0012 airfoil. We now consider the noise due to the two cambered airfoils, NACA4312 and NACA6312, chosen to have identical thickness-to-chord ratios to that of the NACA0012 airfoil but whose camber-to-chord ratio is now 4% and 6% respectively. These three airfoil profiles are shown in Fig. 11.

In this study, we assume that the chordwise and spanwise mean loading distributions remain unaffected by the change in airfoil geometry and hence the tonal radiation due to mean loading for all three NACA airfoils under investigation will be predicted to

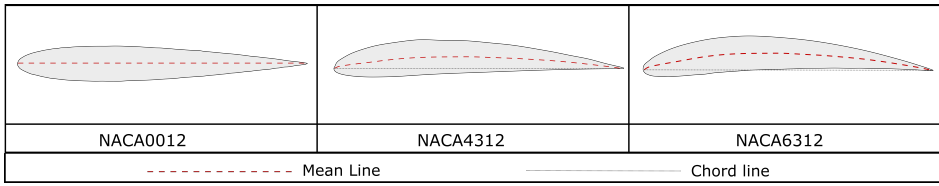


**Figure 11.** NACA airfoils shapes considered for study.

be identical. Moreover, since the thickness of all three airfoils is kept constant, the tonal noise due to thickness is also predicted to be identical. However, since the drag coefficients of these airfoils will differ by virtue of their different geometries, their broadband noise radiation will differ, thereby altering their balance relative to their tonal noise radiation.

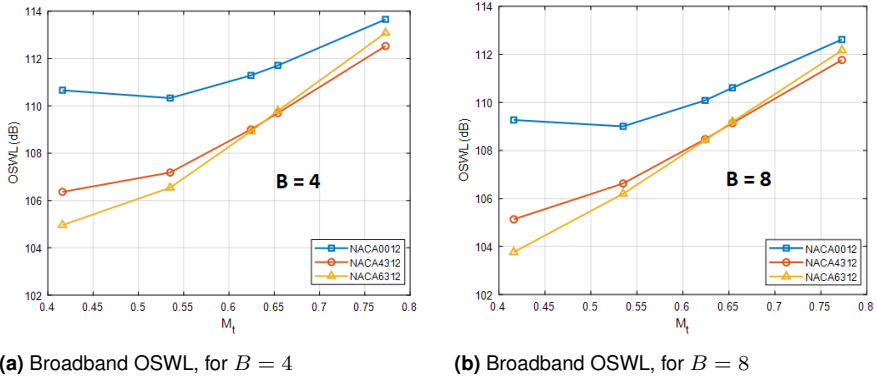


**Figure 12.** Effect of airfoil geometry on the broadband OSWL

Similar to the study for the NACA0012 airfoil propeller presented above, the broadband OSWL were computed for the two cambered airfoils over a range of tip Mach number and blade number. Figures 12a and 12b show the variation in broadband OSWL with blade tip Mach number for the three NACA airfoil geometries for  $B = 4$  and  $B = 8$  respectively. In both cases the overall broadband levels due to the NACA0012 airfoil is highest across the range of  $M_t$  with the greatest difference being observed at

lowest tip speeds where, according to Fig. 6a and Fig. 6b, the broadband spectrum is a significant contributor to the overall noise. The difference in overall broadband levels can be observed to diminish as the tip speed is increased, where at the highest tip speed the broadband levels for the three airfoils varies by more than 2dB. Comparison of the overall noise variation between Fig. 12a and Fig. 12b indicate that, as is well documented, overall broadband noise levels reduce as the the number of blades increases whilst maintaining blade solidity and thrust.

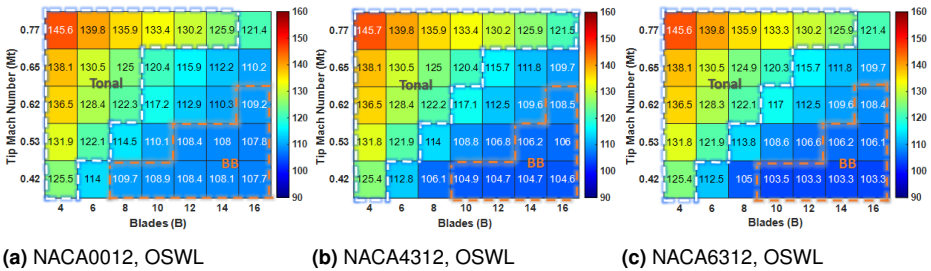


Figure 13. Effect of airfoil geometry on overall noise

The variation in overall broadband noise with airfoil geometry, tip Mach number and number of blades is readily explained by the variation in the trailing edge boundary layer thickness  $\delta$  from which the trailing edge surface pressure spectrum is derived, and hence its subsequent far field radiation. The boundary layer thickness, computed from the panel code XFOIL, is the result of the local angle of attack  $\alpha_a$  and the pressure gradient driven by the airfoil geometry. Calculations of the boundary layer thickness for the three airfoil geometries (not shown here), at the same chord and span, are found to converge as the local flow speed is increased due to increasing tip Mach number. This behaviour is predominantly due to sensitivity of boundary layer thickness to increasing chordwise Reynolds number. Broadband noise levels due to the NACA0012 airfoil are therefore

generally higher than the cambered airfoils due to the higher angles of attack necessary to maintain the specified thrust.

Finally, we present an overview of the variation in total overall noise obtained by summing the tonal and broadband noise levels for the three airfoils under consideration. Fig. 13a, 13c and 12a show colourmaps of the total noise at constant thrust and blade solidity plotted against tip Mach number and number of blades. These results delineate clearly the range of  $M_t$  and  $B$  where tonal noise dominates and where broadband noise is the dominant noise mechanism. At relatively low  $B$  and high  $M_t$  tonal noise can be clearly seen to dominate owing to their much greater modal efficiencies. By contrast, at high  $B$  and low  $M_t$  broadband noise is the dominant mechanism owing to the far greater number of acoustic modes that are able to be generated, as discussed in detail in Section titled “Results for NACA0012 airfoil”. Airfoil geometry can be seen to have a negligible effect on the tonal-dominated region but a much larger influence for large  $B$  and small  $M_t$ , in the region where broadband noise is dominant.

## Experimental validation

### *Experimental set-up and procedure*

In this section we present preliminary experimental data aimed at validating the principles identified above from the numerical investigation. The experimental investigation was conducted on a single propeller rig, which is typical of a mid-size drone, with a blade-chord based Reynolds number of order  $10^5$ . The rig consisted of a rotor powered by a U7-V2.0 KV280 motor from T-Motor, mounted on a MINI45 ATI 6-axis loadcell, capable of producing a maximum thrust of 50 N for the largest rotor diameter and maximum rotor speeds of 8000RPM. The electronic speed controller used was a Master Mezon 135 opto unit. Commercially available Fiala 16x8 (2, 3, 5, 6,

and 7 bladed) with a diameter of 16 inches were used for the investigation. The precise rotational speed of the propellers was measured using an ICP Laser Tachometer sensor.

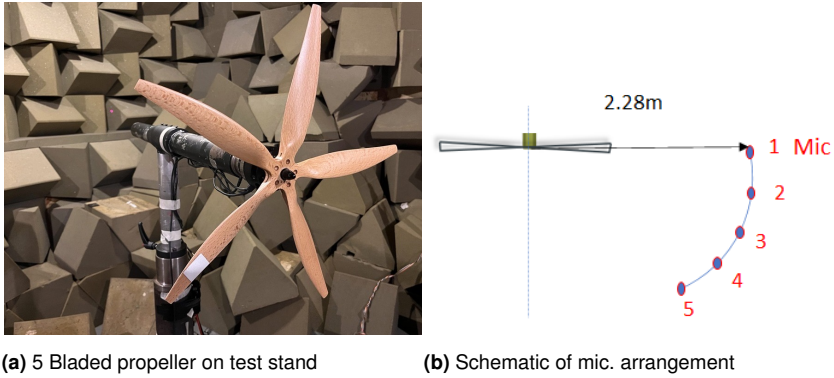


**Figure 14.** Experimental setup and microphone arrangement

Far-field noise measurements on the propeller-wing rig were carried out in the anechoic chamber at the Institute of Sound and Vibration Research (ISVR) with dimensions of 4 m x 4 m x 3 m as shown in Figure 14a. The walls are acoustically treated with foam wedges whose cut-off frequency is estimated to be below 250Hz.

Far-field noise measurements were obtained by using a vertical and a horizontal circular microphone array of 2.28 m radius centred on the propeller rig. The horizontal array consisted of 5 quarter inch GRAS 40PL-10 CCP microphones. A sketch of the microphone arrangement is shown in Figure 14b.

These microphones are placed at emission angles of between  $42^\circ$  and  $90^\circ$  measured relative to the rotor axis. Measurements were carried for 10s duration at a sampling frequency of 40kHz, and the noise spectra was calculated with frequency resolution of 5Hz. Sound Power Level spectra  $PWL(\omega) = 10 \log_{10}(S_w(\omega)/W_{ref})$  was calculated by integrating the Power Spectral Density (PSD) of the acoustic pressure over the 5 microphones. The rotor is placed around 1.5 m above the ground to avoid re-circulation.

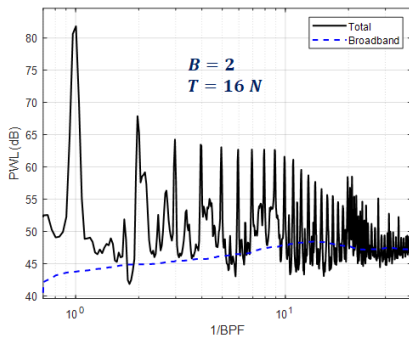
## Experimental results

The balance between the tonal and broadband noise of the propeller was investigated experimentally by measuring the radiated noise of propellers with blade numbers equal to 2, 3, 5, 6, and 7 at a constant thrust of 16N. To maintain the thrust produced by the different propellers, they were operated at the different tip speeds corresponding to tip Mach of  $M_t = 0.27, 0.24, 0.22, 0.21,$  and 0.20, respectively. However, it was not possible to maintain constant blade solidity in these experiments as the range of propellers were limited to those available commercially. It was therefore only possible to interrogate the diagonal elements of the noise matrices shown in Fig.10 and Fig. 13.

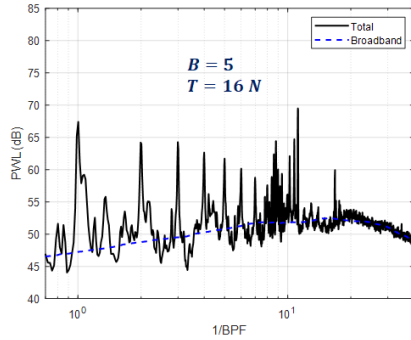
Figure 15 shows the measured Sound Power Level (PWL) frequency spectrum normalised on BPF for a 2-bladed and 5-bladed propeller. The figure shows both the total and broadband components of the measured PWL spectra. The broadband spectra were extracted from the total noise spectra by applying a median filter filter that the noise at every frequency is obtained by from the median value of the noise level at three frequency points either side of it.

Tonal noise is observed to dominate at low frequencies, and broadband noise at higher frequencies. This behaviour is consistent with the predictions shown in Fig. 6. For the 2-bladed propeller, tonal noise drops rapidly with increasing frequency, characteristic of the tonal noise spectrum predicted in Fig. 6. *The rate of decay of measured tonal amplitudes over harmonics of BPF does not match exactly with that predicted, for example, Fig. 6. This is due to some level of in-flow distortion onto the propeller caused by, for example, flow re-circulation in the anechoic chamber.*

The tonal noise spectrum for the 5-bladed propeller can be observed to decay at a slower rate with increasing frequency when compared to the 2-bladed propeller. Furthermore, an increase in tonal noise is further evidence of in-flow distortion. In addition, there is an increase in broadband noise with the increase in blade numbers.

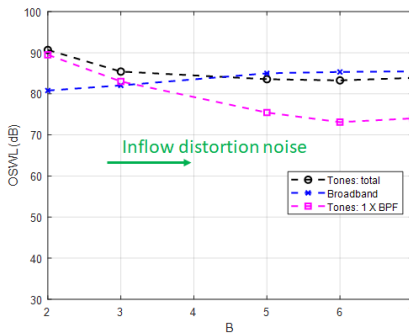


(a) Measured PWL  $B = 2$

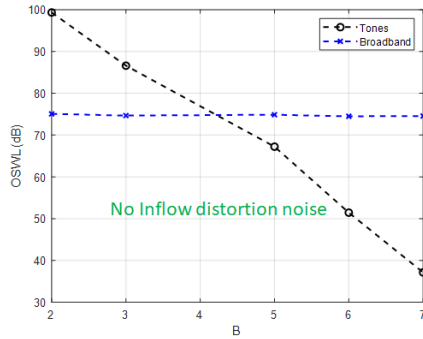


(b) Measured PWL  $B = 5$

**Figure 15.** Measured and predicted overall noise level with its tonal and broadband components for the thrust of 16N



(a) Measured OSWL



(b) Predicted OSWL

**Figure 16.** Measured and predicted overall noise level with its tonal and broadband components for the thrust of 16N

A comparison of the measured and predicted Overall Sound Power Level OSWL versus blade number  $B$  for these measurements are plotted in Fig.16a and 16b, respectively. In Fig.16a, we separately examined tonal noise at  $1^{st}$  BPF and tonal noise summed over all harmonics with the broadband noise. The difference between the tonal noise from the  $1^{st}$  BPF and the total tonal noise increases with an increase in blade

number, providing clear evidence of higher in-flow distortion at higher blade numbers. Ultimately, considering the contributions from the 1<sup>st</sup> BPF alone leads to a shift in the balance between tonal and broadband noise towards lower blade numbers.

The measured overall noise levels show that the broadband noise dominates at higher blade number (and therefore lower tip speed), which is consistent with predictions shown in Fig.10.

To compare the overall trend in predicted noise with measurements, we use approximate geometric (chord distribution and airfoil shape) and aerodynamic information of the propeller to predict its tonal and broadband noise. Furthermore, to maintain consistency, we applied the same assumptions (discussed in previous sections) to broadband noise prediction models regarding the surface pressure spectrum models. The Reynolds number for the propeller under test is likely to be transitional  $O(10^5)$ . At these comparatively low Reynolds numbers the boundary layer over the blades may not be fully turbulent and therefore the current broadband noise models, developed at higher Reynolds numbers, may not be accurate. However, we are encouraged by the good levels of agreement obtained between the self-noise prediction model adopted in this paper and used previously by Blandeau<sup>4</sup> and the measured surface pressure spectrum by Garcia Sagrado<sup>39</sup> at the relatively low Reynolds number of  $O(10^5)$ . Measured overall tonal noise can be observed in Fig.16a to drop by about 6dB as  $B$  is increased from 2 to 3 but then plateaus for values of  $B$  above this. By contrast the predicted overall tonal level drops by about 12dB for  $B$  increasing from 2 to 3 but is predicted to continue dropping at the same rate as  $B$  is increased further.

Trends in the variation in overall broadband noise level with  $B$  are correctly predicted with the measured levels shown to increase by just 3dB by increasing  $B$  from 2 to 6 while the predicted levels remain roughly constant.

---

The marked difference in behaviour of the tonal noise with  $B$  can be attributed directly to the high levels of in-flow distortion noise caused by recirculating flow in the anechoic chamber. This additional noise source is not expected to be as significant in the free field. Measurements of the variations of the overall broadband level are in general agreement with predictions, while the correct trend in the variation in tonal noise is predicted for small blade counts where the tonal self-noise is expected to be significantly higher than the tonal interaction noise due to in-flow distortion.

## Conclusion

This paper has investigated the factors that affect the balance between tonal and broadband noise due to an isolated propeller in uniform motion. Tones are assumed to be due to steady blade loading and thickness, while the broadband noise is assumed to be due to the scattering of the turbulent boundary layer at the trailing edge. One of the objectives of this paper is to highlight the similarities and differences in the theoretical formulations for tonal and broadband noise, thereby allowing the essential differences between them to be identified.

The most significant difference between the mechanisms and character of the tonal and broadband radiation from a propeller has been identified as being due to the number of acoustic modes that are able to be excited at any blade passing frequency in the case of tones, and in a narrow frequency band in the case of broadband noise.

As is well established the tonal noise due to steady blade loading is highly sensitive to blade number and tip speed. This behaviour has been demonstrated to be due to the high sensitivity of the radiation efficiency of the single acoustic mode that is excited at any blade passing frequency. By contrast, broadband noise in a narrow frequency band is considerably less sensitive to blade number and tip Mach number since it excites a range of acoustic modes of varying radiation efficiencies. The overall efficiency of radiation,

therefore, is determined by the radiation efficiency of the most efficient modes, which is generally due to the least cutoff mode. Tonal noise has therefore been observed to be by far the dominant noise mechanisms for low  $B$  and high  $M_t$ , whereas the broadband noise is dominant for high  $B$  and low  $M_t$ . Clearly, therefore, there exists a combination of  $B$  and  $M_t$  for which the two noise mechanisms contribute equally to the overall noise of the propeller. This behaviour of tonal and broadband noise has been confirmed with measured noise results in an anechoic chamber.

This fundamental difference in the number of acoustic modes that can be excited has also been found to be the cause of the difference in directivities of tonal and broadband noise. Tonal noise generally peaks towards the plane of rotation while broadband noise has peak radiation close to the propeller axis.

We note that this study has not considered the tonal noise due to in-flow distortion, which typically tends to dominate at the higher harmonics of BPF. However, in the current anechoic chamber measurements, we observed that, for higher blade numbers, the noise due to in-flow distortion effect is present even at the fundamental BPF and its subsequent harmonics. Therefore, at high blade numbers, we observed considerable discrepancies between measured and predicted tonal noise. This paper has also not considered the contribution from other broadband sources, such as the broadband noise due to inflow turbulence caused by installation effects. Nevertheless, the study has focused on the main tonal and broadband noise generation mechanisms in order to highlight the balance between them, to provide guidance on the design of low noise propellers, and to highlight the fundamental similarities and differences between them.

## Acknowledgements

The authors would also like to thank Rolls-Royce for technical & financial support. Chaitanya Paruchuri would like to acknowledge the financial support of the Royal Academy of Engineering (RF\201819 \ 18 \ 194) in building the propeller rig.

---

## References

1. Farassat F. Derivation of formulations 1 and 1a of farassat. Technical report, 2007.
2. Chirico G, Barakos GN and Bown N. Numerical aeroacoustic analysis of propeller designs. *The Aeronautical Journal* 2018; 122(1248): 283–315.
3. Parry AB. *Theoretical prediction of counter-rotating propeller noise*. PhD Thesis, University of Leeds, 1988.
4. Blandeau V. *Aerodynamic broadband noise from contra-rotating open rotors*. PhD Thesis, University of Southampton, 2011.
5. Akiwate DC, Parry AB, Joseph P et al. On the balance between the tonal and broadband noise of uninstalled propellers. In *AIAA AVIATION 2021 FORUM, 2021*.
6. Drela M. Xfoil: An analysis and design system for low reynolds number airfoils. In *Low Reynolds number aerodynamics*. Springer, 1989.
7. Atr42-500. Brochure, 2021. URL <https://1tr779ud5r1jjgc938wedppw-wpengine.netdna-ssl.com/wp-content/uploads/2020/07/42-500.pdf>.
8. Atr42-600. Brochure, 2021. URL [https://www.atr-aircraft.com/wp-content/uploads/2020/07/Factsheets\\_-\\_ATR\\_42-600.pdf](https://www.atr-aircraft.com/wp-content/uploads/2020/07/Factsheets_-_ATR_42-600.pdf).
9. Klein P. *Parametric modeling and optimization of advanced propellers for next-generation aircraft*. Master's Thesis, Delft University of Technology, 2017.
10. Airbus. Global market forecast: Future journeys 2013-2032. Technical report, Airbus, 2013. URL <http://www.airbus.com/company/market/forecast/>.
11. Kurtz D and Marte J. A review of aerodynamic noise from propellers, rotors, and lift fans. Technical report, NASA 32-1462, 1970.
12. Glegg S and Devenport W. *Aeroacoustics of low Mach number flows: fundamentals, analysis, and measurement*. Academic Press, 2017.
13. Gutin L. On the sound field of a rotating propeller. Technical report, NASA 1195, 1948.

14. Hubbard H, Lansing D and Runyan H. A review of rotating blade noise technology. *Journal of Sound and Vibration* 1971; 19(3): 227–249.
15. Goldstein ME. *Aeroacoustics*. McGraw-Hill International Book Co., New York, 1976.
16. Hanson DB. Helicoidal surface theory for harmonic noise of propellers in the far field. *AIAA Journal* 1980; 18(10): 1213–1220.
17. Hanson DB. Sound from a propeller at angle of attack: a new theoretical viewpoint. *Proceedings of the Royal Society of London Series A: Mathematical and Physical Sciences* 1995; 449(1936): 315–328.
18. Hanson DB. Compressible helicoidal surface theory for propeller aerodynamics and noise. *AIAA Journal* 1983; 21(6): 881–889.
19. Kim Y and George A. Trailing-edge noise from hovering rotors. *AIAA Journal* 1982; 20(9): 1167–1174.
20. Brooks TF, Pope DS and Marcolini MA. Airfoil self-noise and prediction. Technical report, NASA 1218, 1989.
21. Brooks TF and Hodgson T. Trailing edge noise prediction from measured surface pressures. *Journal of Sound and Vibration* 1981; 78(1): 69–117.
22. Blandeau VP and Joseph PF. Validity of amiet’s model for propeller trailing-edge noise. *AIAA Journal* 2011; 49(5): 1057–1066.
23. Gojon R, Jardin T and Parisot-Dupuis H. Experimental investigation of low reynolds number rotor noise. *The Journal of the Acoustical Society of America* 2021; 149(6): 3813–3829.
24. Greenwood E, Brentner KS, Rau RF et al. Challenges and opportunities for low noise electric aircraft. *International Journal of Aeroacoustics* 2022; 21(5-7): 315–381.
25. Amiet RK. Noise due to turbulent flow past a trailing edge. *Journal of Sound and Vibration* 1976; 47(3): 387–393.
26. Amiet R. Effect of the incident surface pressure field on noise due to turbulent flow past a trailing edge. *Journal of Sound and Vibration* 1978; 57(2): 305–306.

- 
27. Rozenberg Y. *Modélisation analytique du bruit aérodynamique à large bande des machines tournantes: utilisation de calculs moyennés de mécanique des fluides*. PhD Thesis, Ecole Centrale de Lyon, 2007.
  28. Kingan M. Advanced open rotor noise prediction. *The Aeronautical Journal* 2014; 118(1208): 1125–1135.
  29. Saravanamuttoo HHH, Rogers G, H Cohen et al. *Gas Turbine Theory*. 7th editio ed. Pearson, 2017.
  30. Stokkermans TC, Nootebos S and Veldhuis LL. Analysis and design of a small-scale wingtip-mounted pusher propeller. In *AIAA Aviation 2019 Forum*, 2019.
  31. Hanson DB and Fink MR. The importance of quadrupole sources in prediction of transonic tip speed propeller noise. *Journal of Sound and Vibration* 1979; 62(1): 19–38.
  32. Roger M and Moreau S. Back-scattering correction and further extensions of amiet’s trailing-edge noise model. part 1: theory. *Journal of Sound and vibration* 2005; 286(3): 477–506.
  33. Rozenberg Y, Roger M and Moreau S. Rotating blade trailing-edge noise: Experimental validation of analytical model. *AIAA Journal* 2010; 48(5): 951–962.
  34. Roger M and Moreau S. Tonal-noise assessment of quadrotor-type uav using source-mode expansions. *Acoustics* 2020; 2(3): 674–690.
  35. Acevedo Giraldo D, Roger M, Jacob MC et al. Analytical study of the aerodynamic noise emitted by distributed electric propulsion systems. In *28th AIAA/CEAS Aeroacoustics Conference 2022*.
  36. Parry A and Crighton D. Asymptotic theory of propeller noise. i-subsonic single-rotation propeller. *AIAA Journal* 1989; 27(9): 1184–1190.
  37. Hwang Y, Bonness WK and Hambric SA. Comparison of semi-empirical models for turbulent boundary layer wall pressure spectra. *Journal of Sound and Vibration* 2009; 319(1-2): 199–217.

38. Baskaran K, Jamaluddin NS, Celik A et al. Effects of number of blades on propeller noise. *Journal of Sound and Vibration* 2023; 572: 118176.
39. Garcia Sagrado AP. *Boundary layer and trailing edge noise sources*. PhD Thesis, University of Cambridge, 2008.

## Appendix

### Nomenclature

$SPL_{\text{Tonal}}$	=	tonal sound pressure level [dB]
$SPL_{\text{BB}}$	=	broadband sound pressure level [dB]
$SS_{pp}^{TE}$	=	broadband far-field power spectral density of acoustic pressure
$SS_{ppj}^{TE}$	=	broadband far-field power spectral density of acoustic pressure for $j^{\text{th}}$ strip
$W(f)$	=	sound power [W]
OSWL	=	far-field overall acoustic sound power level [dB]
PWL( $f$ )	=	far-field sound power level [dB]
BPF	=	blade passing frequency [Hz]
$bw$	=	bandwidth of frequency [Hz]
$\overline{P_m^2}$	=	Tonal mean square sound pressure [ $\text{N}^2 \cdot \text{m}^{-4}$ ]
$P_{ref}^2$	=	reference square sound pressure, $(20 \times 10^{-6})^2$ [ $\text{N}^2 \cdot \text{m}^{-4}$ ]
$c_0$	=	speed of sound [ $\text{m} \cdot \text{s}^{-1}$ ]
$U_r$	=	sectional incoming flow velocity [ $\text{m} \cdot \text{s}^{-1}$ ]
$M_r$	=	sectional Mach number, $M_r = \frac{U_r}{c_0}$
$\rho$	=	density of the medium [ $\text{kg} \cdot \text{m}^{-3}$ ]
$\alpha_a$	=	local angle of attack/incidence [deg]
$\alpha$	=	stagger angle [deg]
$\theta_f$	=	flow angle [deg]
$C_L$	=	lift coefficient
$C_D$	=	drag coefficient

---

$c$	= chord [m]
$T$	= thrust [N]
$\sigma$	= blade solidity
$P_c$	= blade pitch [m]
$\Omega$	= angular speed [rad.s <sup>-1</sup> ]
$f$	= frequency [Hz]
$V_0(r), V_t(r)$	= axial and rotational components of the flow [m.s <sup>-1</sup> ]
$r_0$	= observer distance [m]
$\theta$	= observer polar angle [deg]
$\omega_m$	= tonal angular frequency at $m^{th}$ harmonic, $\omega_m = mB\Omega$ [rad.s <sup>-1</sup> ]
$B$	= blade number
$R_t$	= tip radius [m]
$D_t$	= diameter of propeller [m]
$r_h$	= hub radius [m]
$M_x$	= axial or forward flight Mach number
$\nu$	= azimuthal acoustic mode order
$k_0$	= broadband acoustic wave number, $k_0 = \frac{\omega}{c_0(1-M_x \cos\theta)}$ [m <sup>-1</sup> ]
$D_{\nu M}, D_{\nu L}, D_{\nu D}$	= radiation terms for thickness, loading, and drag noise
$D_{\nu BB}$	= radiation terms for broadband noise
$S(r)_M, S(r)_L, S(r)_D$	= source terms for thickness, loading, and drag noise
$S(r)_{BB}$	= source terms for broadband noise
$J_\nu$	= Bessel function of the first kind of order $\nu$
$m$	= azimuthal harmonic index
$q$	= turbulence azimuthal mode order
$k_m$	= tonal wave number at $m^{th}$ harmonic, $k_m = \frac{\omega_m}{c_0(1-M_x \cos\theta)}$ [m <sup>-1</sup> ]
$b$	= maximum thickness of the blade along a chord position [m]
$\Psi_V$	= non-compactness term for thickness noise
$k(x)$	= chord-wise wave number for tonal noise [m <sup>-1</sup> ]
$\tilde{X} = X/c$	= dimensionless chord-wise co-ordinate
$h(\tilde{X})$	= chord-wise thickness function

$F(\tilde{X})$	= chord-wise lift function
$\frac{dL}{dr}$	= acoustically weighted loading harmonic [ $\text{kg}\cdot\text{s}^{-2}$ ]
$\frac{dD}{dr}$	= acoustically weighted loading harmonic [ $\text{kg}\cdot\text{s}^{-2}$ ]
$j$	= number of strips
$\bar{r}_j$	= span-wise location of the mid-point of the $j^{\text{th}}$ strip [m]
$M_{r_j}$	= sectional Mach number for the $j^{\text{th}}$ strip
$U_c$	= convective velocity in boundary layer, $U_c = 0.8 \times U_{r_j}$ [ $\text{m}\cdot\text{s}^{-1}$ ]
$M_c$	= convective Mach number in boundary layer, $M_c = 0.8 \times M_{r_j}$
$\Delta r$	= radial strip width [m]
$k_r$	= turbulence span-wise wavenumber [ $\text{m}^{-1}$ ]
$K_{X,\nu}$	= turbulence chord-wise wavenumber [ $\text{m}^{-1}$ ]
$\kappa_\nu$	= turbulence aeroacoustic coupling wavenumber [ $\text{m}^{-1}$ ]
$\mathcal{L}^{TE}(k_r, K_{X,\nu}, \kappa_\nu)$	= unsteady loading term due to trailing edge interaction
$g^{TE}(X, k_r, K_{X,\nu}, M_{r_j})$	= flat plate response function due to trailing edge interaction
$SS_{qq}(k_r, K_{X,\nu})$	= spectral density of the surface pressure cross-spectrum [ $\text{kg}^2\cdot\text{m}^{-1}\text{s}^{-3}$ ]
$l_r(K_{X,\nu}U_c, k_r)$	= span-wise correlation length of surface pressure [m]
$\Phi_{pp}(K_{X,\nu}U_c)$	= surface pressure spectrum density [ $\text{Pa}^2\cdot\text{s}$ ]
$\delta^*$	= displacement thickness [m]
$\delta$	= boundary layer thickness [m]
$\tau_\omega$	= wall shear stress, $\tau_\omega = C_f \times 0.5\rho U_r^2$ [Pa]
$C_f$	= skin friction coefficient
$\bar{\omega}$	= $\bar{\omega} = \frac{ K_{X,\nu}U_c \delta^*}{U_X}$
$U_X$	= free stream velocity relative to the chord of the rotor blades [ $\text{m}\cdot\text{s}^{-1}$ ]
$\tilde{\omega}$	= dimensionless frequency
$R_T$	= ratio of outer-to-inner timescales of boundary layer, $R_T = \frac{8\delta^*u_t}{\eta} \sqrt{\frac{C_f}{2}}$
$\eta$	= kinematic viscosity [ $\text{m}^2\cdot\text{s}$ ]
$u_t$	= friction velocity [ $\text{m}\cdot\text{s}^{-1}$ ]
$\Pi$	= Cole's wake law parameter
$\beta_c$	= Clauser's pressure gradient parameter
$\Theta$	= momentum thickness [m]

$$\frac{dp}{dx} = \text{pressure gradient along the chord}$$

## Loading

The total tonal mean square sound pressure produced by the propeller is a sum of mean square pressures by loading  $\overline{P_{mL}^2}$  and  $\overline{P_{mT}^2}$ . This appendix describes the formulation for sound pressure due to loading and thickness noise. The mean square sound pressure  $\overline{P_{mL}^2}$  at the  $m^{\text{th}}$  harmonic of blade passing frequency produced by the loading noise is given by<sup>3</sup>:

$$\begin{aligned} \overline{P_{mL}^2} = & \left( \frac{BR_t}{2\pi r_o (1 - M_x \cos\theta)} \right)^2 \left[ \int_{r_h}^{R_t} \left\{ ik_m \cos\theta \sin\alpha + \frac{i}{r} \nu \cos\alpha \right\} J_\nu(k_m r \sin\theta) S(r)_{dL} dz \right. \\ & \left. + \int_{r_h}^{R_t} \left\{ ik_m \cos\theta \cos\alpha - \frac{i}{r} \nu \sin\alpha \right\} J_\nu(k_m r \sin\theta) S(r)_{dD} dz \right]_{dipole}^2 \end{aligned} \quad (9)$$

The source strengths  $S_{dL}(r)$  and  $S_{dD}(r)$  corresponding to lift and drag forces are as follows

$$\begin{aligned} S_L(r) &= \frac{dL}{dr} \\ S_D(r) &= \frac{dD}{dr} \end{aligned} \quad (10)$$

where  $r = zR_t$ ,  $\nu = mB$  and  $\omega_m = mB\Omega$  is the angular frequency of the  $m$ th harmonic for a propeller with angular shaft speed  $\Omega$ ; the wavenumber  $k_m$  is given by  $k_m = \omega_m/c_0 [1 - M_x \cos\theta]$ . Here,  $\alpha$  is the local stagger angle of the propeller.  $\frac{dL}{dr}$  is an acoustically weighted loading harmonic that includes the chordwise non-compactness and is defined by

$$\frac{dL}{dr} = \frac{1}{2} \rho U_r^2 C_L \int_{-1/2}^{1/2} \exp\{-ik_x \tilde{X}\} F(\tilde{X}) c d\tilde{X} \quad (11)$$

Here,  $\tilde{X} = X/c$  is a dimensionless chordwise co-ordinate and  $k_x$  is a chord-wise wave number,

$$k_x = \left( k_m \cos\alpha \cos\theta - \frac{\nu \sin\alpha}{r} \right) c \quad (12)$$

$F(\tilde{X})$  is a dimensionless chordwise lift function that satisfies

$$\int_{-1/2}^{1/2} F(\tilde{X}) d\tilde{X} = 1 \quad (13)$$

For airfoils with high loading towards leading edge, the chordwise integration evaluated by Parry [2] and the acoustically weighted loading harmonic is given by;

$$\frac{dL}{dr} = \frac{1}{2}\rho U_r^2 c C_L \left[ J_0\left(\frac{k_x}{2}\right) + i J_1\left(\frac{k_x}{2}\right) \right] \quad (14)$$

For compact loading, we have  $k_x \ll 1$  and the acoustically weighted loading can be approximated by

$$\frac{dL}{dr} = \frac{1}{2}\rho U_r^2 c C_L \quad (15)$$

Similar to the lift, the  $\frac{dD}{dr}$  for drag forces considering compact loading is given by;

$$\frac{dD}{dr} = \frac{1}{2}\rho U_r^2 C_D \quad (16)$$

In the current study, the effects of drag forces are assumed to be compact.

**Thickness** Thickness noise mean square tone pressure  $\overline{P_{mT}^2}$  is given by

$$\overline{P_{mT}^2} = \left( \frac{BR_t}{2\pi r_o (1 - M_x \cos\theta)} \right)^2 \left[ \int_{r_h}^{R_t} J_\nu(k_m r \sin\theta) S(r)_{mo} dz \right]_{monopole}^2 \quad (17)$$

Here, the source term  $S(r)_{mo} = i\rho c_0 k_m b U_r \Psi_V$ , where  $b$  is the section maximum thickness. The non-compactness term  $\Psi_V$  is evaluated using by parts and is given by;

$$\Psi_V = ik_x \int_{-1/2}^{1/2} h(\tilde{X}) \exp\{-ik_x \tilde{X}\} d\tilde{X} \quad (18)$$

Here,  $h(\tilde{X})$  is a function that describes the chord-wise thickness distribution, and  $k_x$  is wavenumber along chord defined previously. The non-compact thickness distribution is given by two half-sinusoids as;

$$\begin{aligned} h(\tilde{X}) &= \sin\left(\frac{\pi}{2} \left( \frac{\tilde{X} + 1/2}{X_m + 1/2} \right)\right), \quad \tilde{X} \leq X_m \\ h(\tilde{X}) &= \sin\left(\frac{\pi}{2} \left( \frac{\tilde{X} - 1/2}{X_m - 1/2} \right)\right), \quad \tilde{X} \geq X_m \end{aligned} \quad (19)$$

Here,  $X_m$  is the point of maximum thickness along the chord. Therefore, the  $\Psi_V$  is expressed as;

$$\begin{aligned} \Psi_V = ik_x \left\{ \int_{-1/2}^{X_m} \sin \left( \frac{\pi}{2} \left( \frac{\tilde{X} + 1/2}{X_m + 1/2} \right) \right) \exp \{ -ik_x \tilde{X} \} d\tilde{X} \right. \\ \left. + \int_{X_m}^{1/2} \sin \left( \frac{\pi}{2} \left( \frac{\tilde{X} - 1/2}{X_m - 1/2} \right) \right) \exp \{ -ik_x \tilde{X} \} d\tilde{X} \right\} \end{aligned} \quad (20)$$

Evaluating these integrals along chord leads to

$$\Psi_V = ik_x \left\{ \Psi_V^{(1)} + \Psi_V^{(2)} \right\} \quad (21)$$

Here,

$$\begin{aligned} \Psi_V^{(1)} &= (X_m + 1/2) \exp \{ ik_x/2 \} \frac{\pi/2 - ih_1 \exp \{ -ih_1 \}}{(\pi/2)^2 - h_1^2} \\ \Psi_V^{(2)} &= -(X_m - 1/2) \exp \{ -ik_x/2 \} \frac{\pi/2 - ih_2 \exp \{ -ih_2 \}}{(\pi/2)^2 - h_2^2} \end{aligned} \quad (22)$$

Where,  $h_1 = k_x (X_m + 1/2)$  and  $h_2 = k_x (X_m - 1/2)$

## Broadband Noise

The far-field power spectral density for the  $j^{th}$  strip is given by<sup>4</sup>

$$\begin{aligned} SS_{ppj}^{TE} (r_0, \theta, \omega) = \frac{\pi}{2B} \left( \frac{c_j}{R_t} \right)^2 \left( \frac{BR_t}{2\pi r_o (1 - M_x \cos \theta)} \right)^2 \sum_{\nu=-\infty}^{\infty} D_\nu (\theta, \alpha, \omega) \\ \left| \mathcal{L}^{TE} (k_r = 0, K_{X,\nu}, \kappa_\nu) \right|^2 S_{qq}(0, K_{X,\nu}) \end{aligned} \quad (23)$$

Where,  $B$  is the number of blades,  $c_j$  is chord length for  $j^{th}$  strip,  $\Delta r$  is the strip width, and  $\alpha$  is the stagger angle. The term  $D_\nu$  is the Polar directivity depends on geometry and frequency and is described in section . The  $\mathcal{L}^{TE}$  is the non-dimensional aerodynamic-acoustic coupling integral along the airfoil chord expressed as

$$\mathcal{L}^{TE} (k_r, K_{X,\nu}, \kappa_\nu) = \frac{1}{c_j/2} \int_{-c_j/2}^{c_j/2} g^{TE} (X, k_r, K_{X,\nu}, M_{r_j}) e^{i\kappa_\nu (X+c_j/2)} dX \quad (24)$$

The term  $g^{TE}$  is the flat plate airfoil response function between the incidence boundary layer pressure and pressure jump. The analytical solution to the chord-wise integral of  $\mathcal{L}^{TE}$  with the

response function given by Amiet<sup>25,26</sup> with correction by Roger and Moreau<sup>32</sup> to consider the effect of skewed gust is given by

$$\mathcal{L}^{TE}(k_r, K_{X,\nu}, \kappa_\nu) = \frac{e^{2i\theta_b}}{i\theta_b} \left\{ e^{-2i\theta_b} \sqrt{\frac{\theta_a}{\theta_a - \theta_b}} \operatorname{erf} \left[ \sqrt{2i(\theta_a - \theta_b)} \right] - \operatorname{erf} \left[ \sqrt{2i\theta_a} \right] + 1 \right\} \quad (25)$$

Where,

$$\begin{aligned} \theta_a &= \frac{c_j}{2} (K_{X,\nu} + \mu_{a\infty} + \mu_a M_{rj}) \\ \theta_b &= \frac{c_j}{2} (|K_{X,\nu}| + |\kappa_\nu|) \end{aligned} \quad (26)$$

Here  $\mu_a = \frac{K_{X,\nu} M_c c_j}{[2(1 - M_{rj}^2)]}$  is acoustic reduced frequency,  $M_c = 0.8 M_{rj}$  is convective Mach number in the turbulent boundary layer,  $K_{X,\nu} = \frac{\omega(1 - M_x \cos\theta) + \nu\Omega}{U_c}$  is the chordwise wavenumber,  $\kappa_\nu = \frac{\nu}{r_j} \sin\alpha - k_0 \cos\alpha \cos\theta$  is the aeroacoustic coupling wave number,  $\nu$  is azimuthal acoustic order. The term  $\mu_{a\infty}$  is defined based on gust as

$$\begin{aligned} \mu_{a\infty} &= \sqrt{\mu_a^2 - \left[ k_r c_j / \left( 2\sqrt{1 - M_{rj}^2} \right) \right]^2} & \text{for} & \quad \frac{K_{X,\nu} M_c}{k_r \sqrt{1 - M_{rj}^2}} > 1 \\ \mu_{a\infty} &= \sqrt{\left[ k_r c_j / \left( 2\sqrt{1 - M_{rj}^2} \right) \right]^2 - \mu_a^2} & \text{for} & \quad \frac{K_{X,\nu} M_c}{k_r \sqrt{1 - M_{rj}^2}} < 1 \end{aligned} \quad (27)$$

The  $SS_{qq}$  is the wavenumber spectral density of the surface pressure cross-spectrum, given by

$$SS_{qq}(k_r, K_{X,\nu}) = \frac{1}{\pi} l_r(K_{X,\nu} U_c, k_r) \Phi_{pp}(K_{X,\nu} U_c) \quad (28)$$

Where,  $l_r(\omega, k_r) = \frac{l_2(\omega)}{\pi} \frac{1}{1 + l_2^2(\omega) k_r^2}$  is spanwise correlation length, the term  $l_2(\omega)$  defined as  $l_2 = \frac{\zeta_2 U_c}{\omega}$ , where  $\zeta_2$  is an empirical constant.  $\Phi_{pp}$  is the surface pressure spectral density close to the trailing edge given by the semi-empirical Rozenberg model as

$$\Phi_{pp} = \frac{1}{2} \frac{\tau_w^2 \delta^*}{U_r} \frac{C\bar{\omega}^2}{[\bar{\omega}^{0.75} + 0.105]^{3.7} + [3.76 R_T^{-0.57} \bar{\omega}]^7} \quad (29)$$

Here  $\delta^*$  is the displacement thickness at the trailing edge,  $\bar{\omega} = \frac{|K_{X,\nu} U_c| \delta^*}{U_x}$ ,  $\tau_w = C_f \times 0.5 \rho U_r^2$  is wall shear stress,  $C_f$  is skin friction coefficient.  $R_T = \left( 8\delta^* \frac{u_r}{\eta} \right) \sqrt{\frac{C_f}{2}}$  is the ratio of outer-to-inner time scales, and  $\eta$  is kinematic viscosity. The term  $u_t = \sqrt{\frac{\tau_w}{\rho_0}}$  is the friction velocity. The

factor  $C = 0.78(1.8 \Pi \beta_c + 6)$  is used to capture the effects of the pressure gradient on the surface pressure spectrum. Here  $\Pi$  is Cole's wake law parameter and  $\beta_c$  is Clauser's pressure gradient parameter estimated given by expressions

$$2\Pi - \ln(1 + \Pi) = \kappa \frac{U_r}{u_t} - \ln\left(\delta^* \frac{U_r}{\eta}\right) - 5.1\kappa - \ln(\kappa) \quad (30)$$

$$\beta_c = \left(\frac{\Theta}{\tau_w}\right) \frac{dp}{dx} \quad (31)$$

where  $\kappa = 0.41$  is the Von Karman constant and  $\frac{dp}{dx}$  is the pressure gradient along the chord. For the current study,  $\frac{dp}{dx}$  is calculated as the average pressure gradient of the pressure coefficient between 50% and 85% of the chord. However, the pressure gradient is estimated from the XFOIL code.